Hypernuclear physics history and some results (JLab Hall A)

(G.M. Urciuoli)

The very beginning: the Magnetic Multi Purpose Spectrometer

IEEE TRANSACTIONS ON MAGNETICS, VOL. 28, NO.1, JANUARY 1992 581

A Magnetic Multi Purpose Spectrometer

S. Frullani, F. Garibaldi, F. Ghio, M. Jodice, G.M. Urciuoli
Physics Laboratory, Istituto Superiore di Sanita'
Istituto Nazionale di Fisica Nucleare Sezione Sanita'
Viale Regina Elena 299, 00161 Roma, Italy
R. De Leo
Physics Department, Universita' di Lecce
Istituto Nazionale di Fisica Nucleare Sezione di Lecce
K. I. Blomqvist
Institut für Physik, Mainz University, 6500 Mainz, Germany
M. Nervi, M. Repetto
Dipartimento di Ingegneria Elettrica
Universita' di Genova, Via Opera Pia 11a, 16145 Genova, Italy

Abstract - The very high quality and precision of the CEBAF beam will allow the investigation of hypernuclear systems with high accuracy and resolution provided the appropriate experimental equipment is implemented. A possible design of a 1.3 GeV/c, high resolution, short-orbit kaon spectrometer, to be used in combination with one of the two 4 GeV/c CEBAF Hall A spectrometer is presented. The facility is a multipurpose one, serving also as a second hadron arm with the capability of going out of the scattering plane and also serving as an electron spectrometer for large scattering angles.

I. INTRODUCTION

The Continuous Electron Beam Accelerator Facility (CEBAF), currently under construction in Newport News, Virginia is a basic nuclear physics research facility, dedicated to study nuclear structure using electron and photons as probes. It will provide a low emittance, 200 μA electron beam with energies up to 4 GeV and 100% duty factor in the three experimental halls simultaneously.

The core experimental equipment for Hall A is a pair of identical superconducting, 4 GeV/c, High Resolution Spectrometers (HRS) [1]. HRS with their optical length of 23 meters are not suitable for detect unstable hadrons as kaons ($c\tau_K$ = 3.7 meters) and low momentum pions, and to measure non-coplanar reactions. Both these requirements imply the use of a relatively short spectrometer whose maximum analysable momentum must be lower than HRS, if the high resolution characteristics have to be preserved. Moreover, a third magnetic spectrometer allows the possibility to perform high resolution, high luminosity triple coincidence experiments in the case that two hadrons in the final state are angularly correlated.

The presented Multi Purpose Spectrometer (MPS) could give to Hall A all these three capabilities making possible the study of new fields in electromagnetic nuclear physics as the out-of-plane reactions, particle correlations and electromagnetic kaon physics probing strange quark behaviour in nucleons and nuclei.

The basic layout of the MPS is shown in Fig. 1. It is a vertical QDQ design including a room temperature Collins type quadrupole followed by a 3.2 meters long dipole magnet with focusing entrance and exit faces. Subsequent to the dipole is another room temperature conventional type quadrupole. The main design characteristics for the MPS are listed in Table I below.

Table I. Main Characteristics of the 1.3 GeV/c QDQ Design

Type	QDQ
Configuration	vertical
Bending angle	75^0
Optical length (m)	10.6
Transverse focusing	point-to-point
Momentum range (Gev/c)	0.2 to 1.3
Momentum acceptance (%)	15
Momentum dispersion (D, cm/%)	9.11
Momentum resolution (est.)	$<10^{-4}$
Radial linear magnification (M)	-1.04
| D/M | (cm/%)	8.76
Angular acceptance : horiz. (mr)	±75
Angular acceptance : vert. (mr)	±75
Angular resolution : horiz. (mr)	~.6
Angular resolution : vert. (mr)	~.6
Solid angle (msr)	19
Transverse length acceptance (cm)	±3
Transverse position resolution (cm)	~0.02

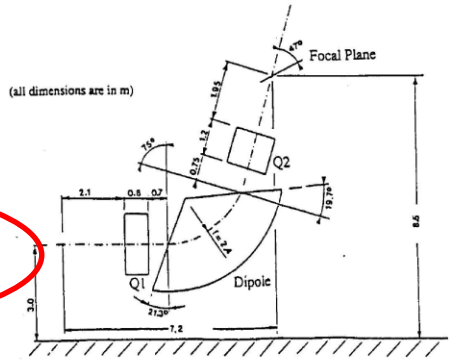

Fig. 1. General layout of the QDQ 1.3 GeV/c spectrometer.

experimental room with the companion High Resolution Spectrometer.

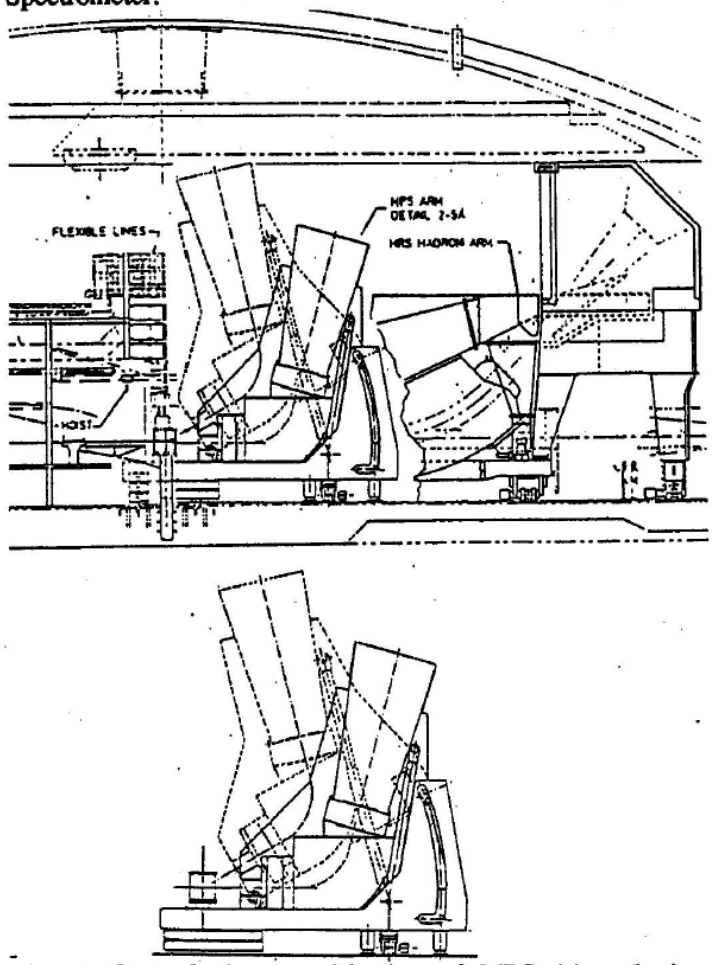

Fig. 7. Out of plane positioning of MPS (a) and its integration in the CEBAF Hall A (b).

Second step: the E94-107 experiment proposal

High Resolution Hypernuclear 1p shell Spectroscopy

S. Frullani, F. Garibaldi
ISS and INFN/Sanita', Rome, Italy
P. Markowitz
University of Maryland, College Park, Maryland
T. Saito
Tohoku University, Japan

Hall A Collaboration Proposal

MIT, Cambridge Massachusetts *INFN/Bari, Bari, Italy*
INFN/Lecce, Lecce, Italy
The University of Virginia, Charlottesville, Virginia
Yerevan Physics Institute, Yerevan, Armenia
University of Georgia, Athens Georgia
American University, Washington
Rutgers University, New Jersey
The College of William and Mary, Williamsburg, Virginia
California State University, California
University of New Hampshire, New Hamphire
Norfolk State University, Norfolk, Virginia
Hampton University, Hampton, Virginia
Nuclear Physics Institute , 25068 Rez/Prague, Czech Republic

December 15, 1994

Current:	Targets:	Beam Energies:	Beam Time:
100 μA	Solid, Waterfall	4 GeV	580 hours

Excerpt from the abstract of the proposal

To obtain maximum cross section, the electron scattering angle has to be as small as possible (large virtual photon flux) and kaon angle close to the virtual photon direction where the moemntum transfer is minimum. This means that it is s a crucial requirement to have $\Theta_e <$ 10°, and $|\Theta_k - \Theta_\gamma| < 10°$.

Kinematical conditions

E_i (GeV)	4
E_o (GeV)	1.8
Θe (°)	6
$\Delta E/E$ (%)	± 5
$\Delta\Omega_e$ (msr)	4.5
p_k (GeV)	1.96
$\Delta p/p$ (%)	± 5
Θ_k (°)	6
$\Delta\Omega_k$ (msr)	4.5
N_e	6.2×10^{24}
target thickness (mg/cm2)	100
K surv. prob. (%)	18

Energy resolution assuming a momentum dispersed beam

Source		*Error*
primary beam	(2×10^{-4} of 4 GeV)	80 keV
outgoing electron	(10^{-4} of 1.8 GeV)	180 keV
outgoing kaon	(10^{-4} of 1.96 GeV)	190 KeV
kaon straggling on split target	40 KeV	40 keV
Total		280 keV

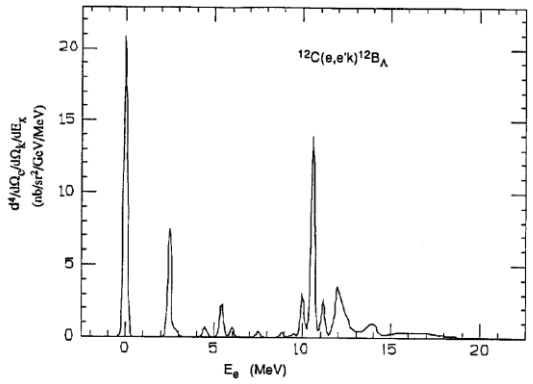

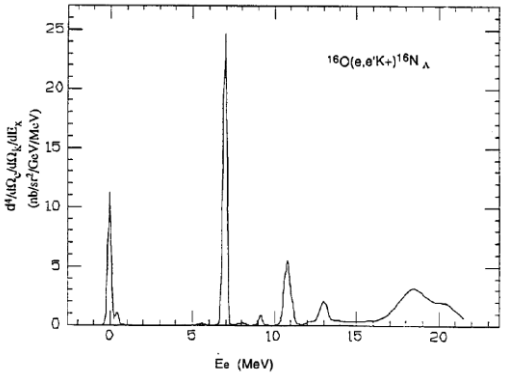

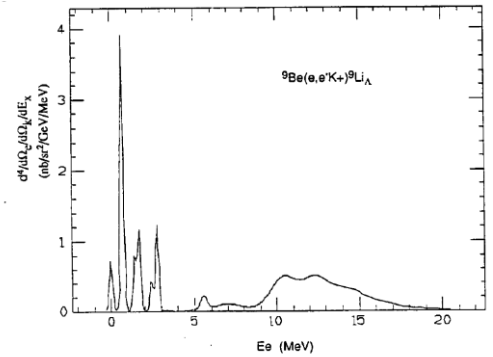

Excerpt from the proposal (kinematical conditions and expected spectra in an ideal case)

To run experiment E94-107:
Hardware implements were needed

To analyze E94-107 data:
innovative algorithms were ideated

Hardware implements
(two septa and a RICH detector)

Septum conceptual design:

The septa were designed to serve not only hypernuclear spectroscopy experiments but also prospective experiments that detected particle scattered from 6° to 12.5°. They were the first septa ever used at JLab $\theta = 6°$

	HRS	HRS(a)	Septum	Septum(r)
Angular acceptance	7.3 msrd	5.5 msrd	4.5	3.4
Momentum resolution	1.0×10^{-4}	2.0×10^{-4}	1.2×10^{-4}	2.0×10^{-4}
Minimum scattering angle	12.5°	12.5°	6°	6°
Momentum Range	0.4-4 GeV/c	0.4-4 GeV/c	0.4-4 GeV/c	0.4-4 GeV/c

Excerpt from the proposal of two septum magnets for forward angle physics in Hall A

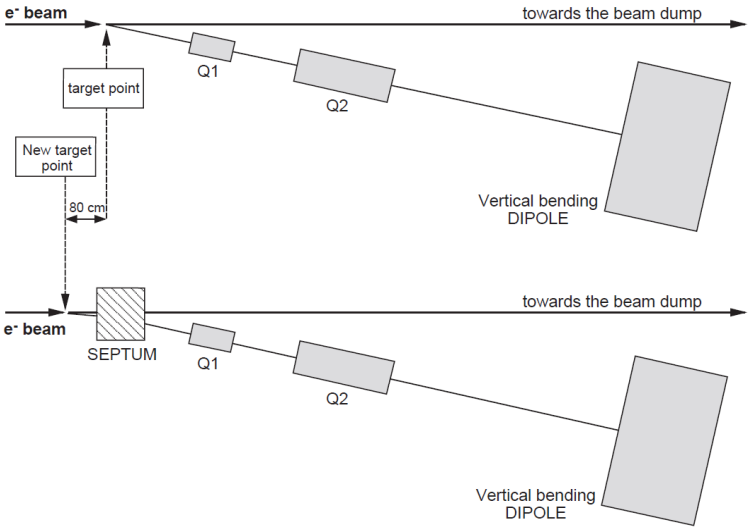

The septum shape was almost completely determined by two parameters: the distance d between the old and the new position of the target (80 cm), and the magnet thickness T between the septum gap and the beam pipe, (2.5 cm.).

d determined:

1 The angular acceptance, that is equal to the HRS original design scaled by the factor D/135 (D is the length in cm of the trajectory between the new target and Q1, 135 cm is the distance between the old target and Q1). A bigger value of d allows a longer septum but decreases the angular acceptance.
2 The position of the center of the septum that is given by the intercept of the lines originating from the old (O) the new (O') scattering chamber center (in the case of Figure above, making angles θ = 6° and ϕ = 12.5°, respectively, with the beam direction)
3 The dimension of the gap that accepts all particles scattered in the acceptance cone.
4 The value of the integral of the septum magnetic field along the trajectory that is proportional to the bending angle β = ϕ - θ should be, for obvious reasons, the smallest available value. When θ is close to 6° , ϕ is equal to 12.5 . At higher θ values, ϕ had to be greater than that and required, as a consequence, very high fields and superconducting coils

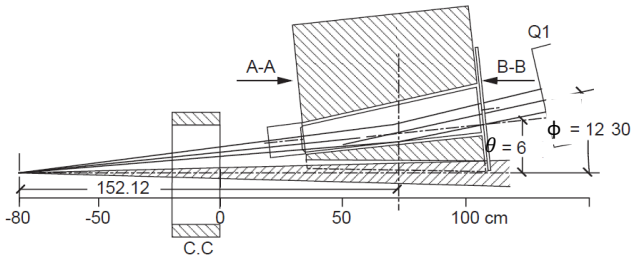

T, the magnet thickness between the gap and the beam pipe, determines, together with d, the septum physical length, L. L should be as long as possible because it is proportional to the integral of the magnetic field inside the septum. The longer L, the lower the required field inside the septum and, hence, the current density needed in the septum coils. L cannot exceed, however, the value that makes the septum edge hit the beam pipe. For this reason T should be as small as possible. The limit is give by the thickness of the coils, the dimension of the cryostat and the thickness of the iron between the coils and the beam pipe (it is needed to ensure good mechanical resistance and good magnetic field homogeneity inside the septum.

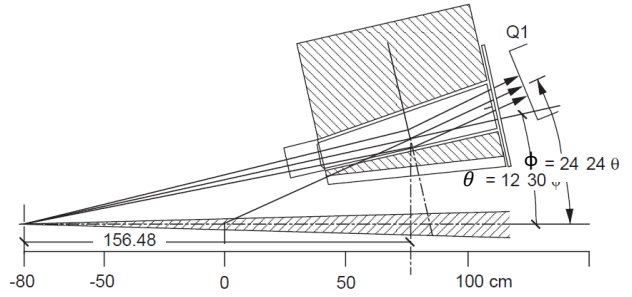

At θ values close to 12.5° , the limit is reached for ϕ because the septum approaches the Q1 edge. High magnetic fields are needed inside the septum. It is useless to decrease the length of the septum in order to allow smaller values of ϕ: the smaller value of the bending angle β = ϕ - θ never compensates, from the magnetic from the magnetic field value point of view, the reduced length of the septum. L is therefore, as explained above, fixed by the geometrical layout at θ = 6° or, in other words, by d and T

Septum technical design

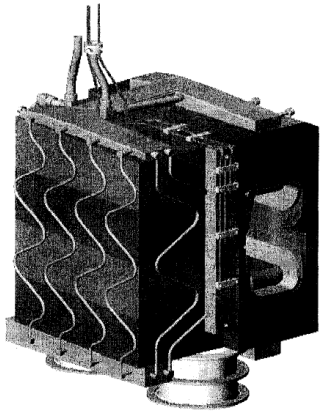

Fig. 4 Septum Magnet Cold Mass, Iron Yoke, Thermo-syphon Cooling Loops, Support Posts and Cold Bus.

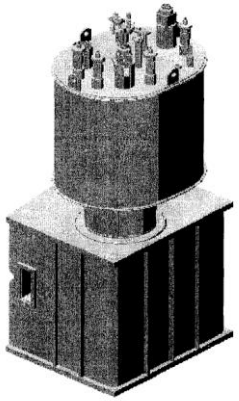

Fig. 3 External View of Septum Magnet Cryostat and Cryo-Reservoir E

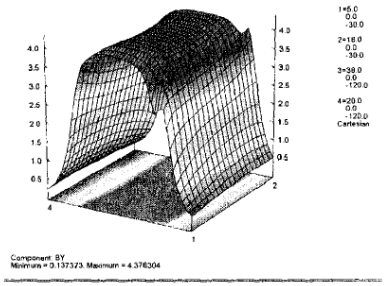

Fig. 1 Mid-Plane Histogram of By at 12.0 degree setting. Current density of 24,000 amps/cm^2.

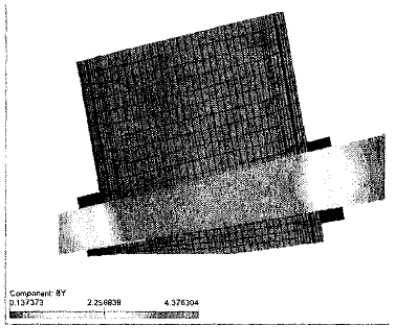

Fig. 2 Mid-Plane Map of By at 12.0 degrees excitation

A semi ordered winding, potted window frame type coil of 709 turns per pole supported by the cold iron yoke.

Coil indirect cooling by conduction through the yoke.

The Superconductor was a single strand 1400 amp conductor operating at 665 amps with a Copper to superconductor ratio of 1.75:1 and Formvar coating

The RICH detector

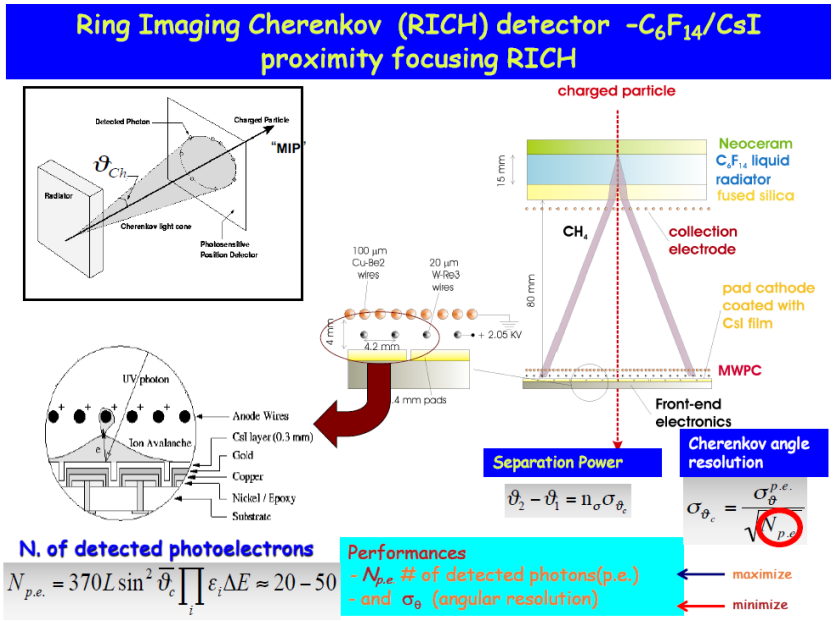

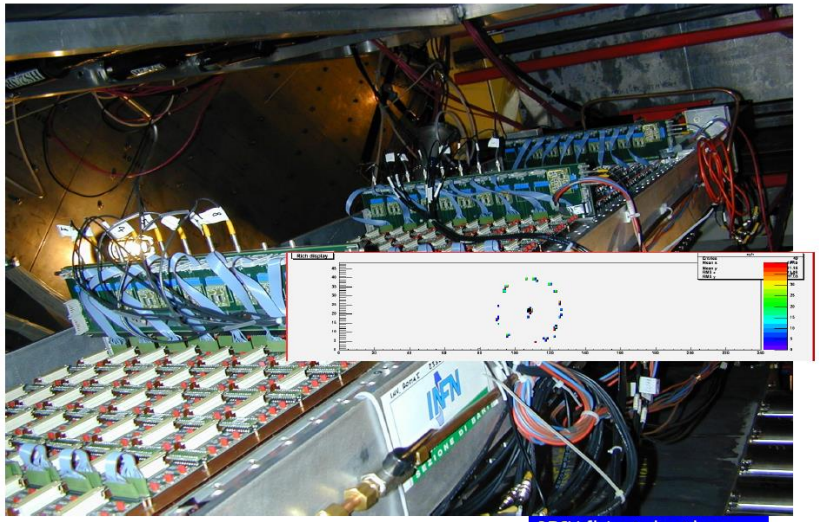

RICH flying to hunt kaons into the detector hut

When a particle crossed the RICH, Cherenov photons were generated in a 15 mm thick liquid perfluorohexane radiator. The photon passed through 5 mm thick quartz slabs placed on the radiator exit window to propagate in a 10 cm proximity gap filled with methane. The photons finally hit three pad planes that made up the cathode of a 2 mm gap Multi Wire Proportional Chamber (MWPC). A 300 mm thick CSI layer on the top of the three pad planes acted as photon converter with a quantum efficiency of ~ 20% around the wave length of λ = 160 nm. The electron migrated to the anode wire plane (at 2 mm from the pads) amplified by an avalanche in the high field at the anode wire. The corresponding signal from this avalanche was collected by the 11520 pads (8x8.4 mm^2 each). As a consequence, a Cherenkov photon generated a cluster of contiguous fired pads "centered" around the avalanche at the wire. From the position of the cluster barycenter, the Cherenkov angle of the photons emitted by the particle.

Innovative algorithms were ideated to address very difficult issues during the hypernuclear spectroscopy experiment analysis:

a) Use of the elementary reactions $p(e,e')\Lambda$ and $p(e,e')\Sigma^0$ to calibrate binding energy spectra

b) Calibration of instruments based on the fulfilment of physical laws to optimize Hall A HRS spectrometer databases

c) Simultaneous checks of the variance and the average of measurements to obtain an effective Particle Identification system with the RICH detector.

d) An innovative radiative correction method to clearly observe difficult to separate peaks in binding energy spectra.

Use of the elementary reactions $p(e,e')\Lambda$ and $p(e,e')\Sigma^0$ to calibrate binding energy spectra

In an experiment performed in Hall A, the energy of the primary electron beam and the central momenta and angles of the two HRSs, by which you determine the scattering angles and the momenta of the scattered particles are constant during all the experiment. However, their values are affected by uncertainties and if they differ by the nominal values set by the experiment kinematics your apparatus is uncalibrated.

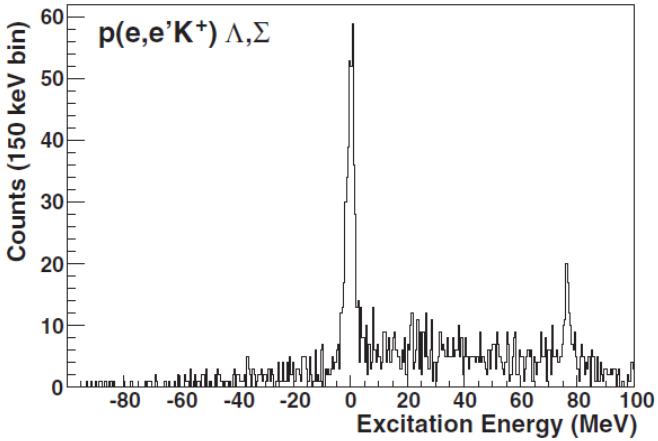

FIG. 14. Excitation energy spectrum of the $p(e,e'K^+)\Lambda, \Sigma^0$ on hydrogen used for energy-scale calibration. The fitted positions (not shown on the plot) for the peaks are -0.04 ± 0.08 MeV and 76.33 ± 0.24 MeV.

The apparatus can be nevertheless calibrated using the elementary reactions $p(e,e')\Lambda$

Defining: $E_H = E_e - E_{e'} - E_k$ $\quad$ $\vec{p}_H = \vec{p}_e - \vec{p}_{e'} - \vec{p}_k$

e the primary electron, *e'* the scattered electron, *k* the produced kaon

If we plot the histogram of $E_{bind} = M_\Lambda - \sqrt{E_H^2 - p_H^2}$ and the acceptance of your spectrometer is adequate, you will obtain two peaks corresponding to Λ and Σ^0 production respectively. The first peak should be centred at 0, the second at a value equal to the difference between the Σ^0 and Λ masses. If this does not happen your apparatus is not calibrated. In this case, you change during the analysis the values of the primary electron beam and the central momenta and angles of the two HRSs in order to locate the two peaks at the right positions. When this two peaks appear at the right positions, your apparatus is calibrated.

Calibration of instruments based on the fulfilment of physical laws to optimize Hall A HRS spectrometer databases

It could happen that one is uncertain about the fact the instrument he is using is calibrated. This could be a problem if no sample of a precise known value of the physical quantity the instrument is measuring is available to calibrate the instrument. This is always the case when one deal with magnetic spectrometers. To overcome this issue we made use of the property that an instrument is calibrated if and only if a physical law that involves the physical quantity our instrument is measuring is fulfilled

Definition of a measuring instrument:

A measuring instrument is a device that measures a physical quantity Y pertaining a determinate object by providing a response X related to the physical quantity value by a mathematical expression E(X):

$$Y = E(X)$$

For example: a mechanical weighing scale that provides us the mass M ≡ Y of an object by its spring deflection X that occurs when the object is placed on it. E(X) is assumed by us.

Definition of a not calibrated measuring instrument:

A measurement instrument is uncalibrated if the real mathematical expression R(X) that connects its response to the values of the physical quantity to be measured is different from the mathematical expression E(X) we assume for it.

$$R(X) \neq E(X)$$

A check of a physical law which involves a physical quantity Y whose values are provided by an uncalibrated measuring instrument will not be of course fulfilled. The difference between the obtained response and the expected one will be however a precise function F[R(X) - E(X)] and because, by definition of measuring instrument, E(X) is always invertible from F[R(X) - E(X)] we can derive R(X) and hence calibrate the measuring instrument.

A simple example:

A weighing scale which measures masses M and for which

$E(X) = \alpha \cdot X$; $R(X) = \alpha' \cdot X + \beta \cdot X^2 + \gamma$; α, α', β, and γ constant,

and hence: $M_{measured} = \alpha \cdot X \neq M_{real} = \alpha' \cdot X + \beta \cdot X^2 + \gamma$

A check of Newton's law $F = M \cdot A$

(F force applied on an object of mass M, and A the acceleration of the object)

will show the "unexpected" law

$$F = M_{real} \cdot A = \left(\frac{\alpha'}{\alpha} \cdot M_{measured} + \frac{\beta}{\alpha^2} \cdot M_{measured}^2 + \gamma\right) \cdot A$$

Observing this false dependence of F on M, we are able to immediately calibrate our weighing scale, in other words to determine $R(X)$. In fact, because $M_{measured} = \alpha \cdot X$, we obtain

$$F = (\alpha' \cdot X + \beta \cdot X^2 + \gamma) \cdot A \longrightarrow M_{real} = \alpha' \cdot X + \beta \cdot X^2 + \gamma$$

$$\longrightarrow \quad R(X) = \alpha' \cdot X + \beta \cdot X^2 + \gamma$$

It is better to write Newton's law in a form more useful for calibrating magnetic spectrometers:

$$L(F, M, A) = F - M \cdot A = 0$$

In case of our uncalibrated weighing scale we have :

$$L(F, M, A) = F - M_{real} \cdot A - (F - M_{real} \cdot A - F + M_{measured} \cdot A) = 0 + A \cdot (M_{real} - M_{measured}) = A \cdot \left(\left(\frac{\alpha'}{\alpha} - 1 \right) \cdot M_{measured} + \frac{\beta}{\alpha^2} \cdot M_{measured}^2 + \gamma \right) = A \cdot P(M_{measured})$$

Or, in other words:

$$L(F, M, A) = A \cdot P(M_{measured}) \neq 0 \quad (1)$$

$P(M_{measured})$ is a polynomial in $M_{measured}$. Our weighing scale is calibrated if and only if

$$P(M_{measured}) = 0 \quad (2)$$

In case of an uncalibrated weighing scale, that is $P(M_{measured}) \neq 0$, to calibrate it we have just to remember that, by definition, $P(M_{measured}) = M_{real} - M_{measured}$ and hence:

$$M_{real} = M_{measured} + P(M_{measured}) \quad (3)$$

Expressing $M_{measured}$ as $M_{measured} = E(X)$ we obtain:

$$M_{real} = E(X) + P(E(X)) = R(X) \quad (4)$$

$$M_{real} = \left(\left(\frac{\alpha'}{\alpha} - 1 \right) \cdot M_{measured} + \frac{\beta}{\alpha^2} \cdot M_{measured}^2 + \gamma \right) + \alpha \cdot x = \alpha' \cdot x + \beta \cdot x^2 + \gamma = R(x)$$

In all the calibration procedure I id not care at all about E(X). I just experimentally determined $P(M_{measured})$. I used E(X) just at the very end to obtain R(X). I can determine M_{real} through (3) even not knowing $R(X)$!!!

Magnetic spectrometer calibration, that is optical data base optimization

In a magnetic spectrometer scattering variables are connected to focal plane coordinates through the equation:

$$\vec{Y} = T \cdot \vec{X} \qquad (5)$$

With T
optical database

$$\vec{Y} = \begin{pmatrix} \delta \\ y_0 \\ \vartheta_0 \\ \varphi_0 \end{pmatrix}$$

δ he percentage difference between the particle momentum and the momentum of the spectrometer central trajectory, y_0 the position along the target of the particle scattering point, and ϑ_0 and φ_0 the particle scattering angles

$$\vec{X} = \begin{pmatrix} x_f \\ y_f \\ \vartheta_f \\ \varphi_f \end{pmatrix}$$

x_f and y_f particle coordinates at the focal plane ϑ_f And φ_f angles that define the particle trajectory when it hits the focal plane

Equation (5) has the form $Y_i = \sum_{klmn} T_{iklmn} \cdot (X_1)^k \cdot (X_2)^l \cdot (X_3)^m \cdot (X_4)^n$

I ,k ,l, m, and n on negative integer numbers

Putting aside mathematical difficulties, equation (5) is completely equivalent to the equation Y=E(X) which connected measured masses Y and weighing scale responses X of the weighing scale.

Five physical laws of the kind $L(Y_1, Y_2, Y_3, Y_4) \equiv L(\delta, y_0, \theta_0, \varphi_0) = constant$ where analyzed:

$$L(\delta, \theta_0, \varphi_0) \equiv E' - \frac{E_0}{1 + \frac{E_0}{M} \cdot (1 - \cos(\Theta))} = 0 \quad (1)$$

Elastic scattering law (E_0 and E' particle energy before and after being scattered, Θ, scattering angle, M target mass)

$$\theta_0 = constant_\theta \quad (2)$$
$$\varphi_0 = constant_\varphi \quad (3)$$

to be fulfilled by the angles θ_0 and φ_0 which define the direction of scattered particles, when a sieve slit is placed in front of the magnetic spectrometer in order to make it detect particles scattered only at defined couple of angles $(constant_\theta, constant_\varphi)$

$$y_0 = constant_y \quad (4)$$

to be fulfilled when particles scatter off a point-like target, positioned at a definite position $constant_y$

$$E_{bind_n} = constant_n \quad (5)$$

E_{bind_n} the binding energy of the n^{th} energy state of a nucleus/hypernucleus

The whole magnetic spectrometer calibration method consisted in observing the possible experimental existence of equation like

$$L(\delta, y_0, \theta_0, \varphi_0) = constant + P(\delta, y_0, \theta_0, \varphi_0)$$

With $P(\delta, y_0, \theta_0, \varphi_0)$ a polynomial in δ, y_0, θ_0, and φ_0.

The calibration was straightforward. For example from (2)

$$\theta_{real}(x_f, y_f, \theta_f, \varphi_f) \equiv constant_\theta = \theta_{0_{measured}}(x_f, y_f, \theta_f, \varphi_f) - P(\delta_{measured}, y_{0_{measured}}, \theta_{0_{measured}}, \varphi_{0_{measured}})$$

To be noted: $\delta_{measured} \equiv \delta_{measured}(x_f, y_f, \theta_f, \varphi_f)$; $y_{0_{measured}} \equiv y_{0_{measured}}(x_f, y_f, \theta_f, \varphi_f)$ etc.

Two results

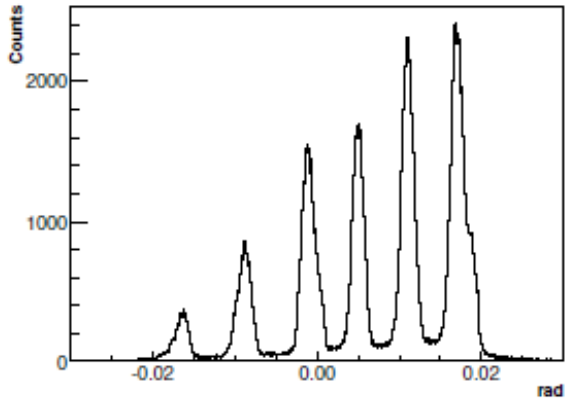

$\varphi_{0_{measured}}$ as determined by the uncalibrated (not optimized) database

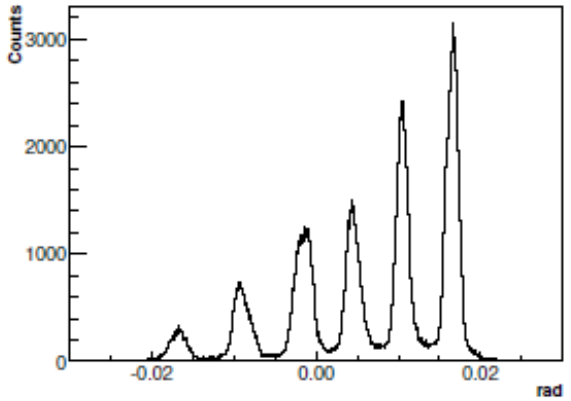

$\varphi_{0_{real}}$ as determined by the equation: $\varphi_{0_{real}} = \varphi_{0_{measured}} - 0.042 \cdot \delta_{measured} - 0.57 \cdot {\delta_{measured}}^2 - 0.002 \cdot \theta_{0_{measured}} + 0.8 \cdot {\theta_{0_{measured}}}^2 + 0.18 \cdot y_{0_{measured}} - 15.9 \cdot {y_{0_{measured}}}^2 + 1.3 \cdot \theta_{0_{measured}} \cdot y_{0_{measured}}$

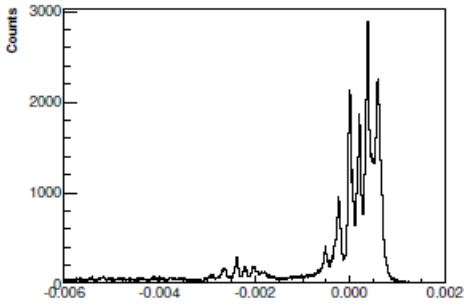

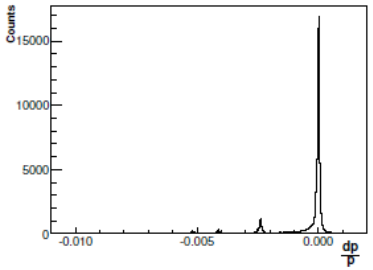

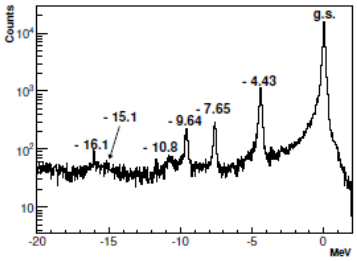

$1 + \delta_{measured} - \frac{P_0}{P_c} \cdot \frac{1}{1+2\cdot\frac{P_0}{M}} \cdot sin^2\left(\frac{\Theta}{2}\right)$

Left: $1 + \delta_{real} - \frac{P_0}{P_c} \cdot \frac{1}{1+2\cdot\frac{P_0}{M}} \cdot sin^2\left(\frac{\Theta}{2}\right)$ with $\delta_{real} = \delta - 0031 \cdot \varphi_{0_{measured}}$; right: the same as left but the abscissa units (MeV) and the ordinate scale (logarithmic). P_0 incident electron momentum, P_c spectrometer central momentum.

$measured \equiv as\ provided\ by\ the\ original\ database$
$real \equiv as\ provided\ by\ the\ optimized\ database$

Simultaneous checks of the variance and the average of measurements to obtain an effective Particle Identification system with the RICH detector.

After a particle crossed the RICH, you have N measurements of the angle the photons it generated trough Cherenkov effect were emitted at. It is important to stress that you do not want to know at what angle the photons were generated but at which angle. In other words you do not have to perform a measurement of the angle but a statistical check that guarantees that the angle is equal to one of possible and already known values. The best way to perform checks is, of course, applying statistical tests in order to quantitatively determine how much an hypothesis about the value of the Cherenkov angle is valid.

Lots of people prefer using Maximum Likelihood Methods to check the consistency of a series of measurements with respect to expected values.

However, a Maximum Likelihood Method never performs better than a method based on a check on the variance of the distribution of the measurements and a check on the variance alone never performs better than a simultaneous check on the variance and on the average of the distribution of the measurements. When the measurements follow a Gaussian distribution, the check on the variance can be easily done with a χ^2 test. This is true for whatever Maximum Likelihood algorithm is employed.

PID based on Maximum Likelihood Method <
< PID based on a χ^2 test <
< PID based on a χ^2 test and on a check of the mean of the measurements.

(ALWAYS!)

In case of measurements following a Gaussian distribution, their variance can be easily checked with a χ^2test.

If the measurements of the Cherenkov angles of the rays of a particle detected by a RICH follow a Gaussian distribution, thus each single measurement X_i, will follow a Gaussian distribution centred around the expected value X_{exp}. Then the sum:

$$Sum = \sum_{i=1}^{N} \frac{(X_i - X_{exp})^2}{\sigma^2{}_{exp}} \qquad (1)$$

follows the χ^2 distribution with N degrees of freedom (no parameter derived by the N measurements).

The sum:

$$\sum_{i=1}^{N} \frac{(X_i - X_{exp})^2}{\sigma^2{}_{exp}} \qquad (1)$$

has N degrees of freedom, because no parameter has been deduced from the measurements X_i, as the value of X_{exp} has been supposed by us and $\sigma^2{}_{exp}$ has been deduced by previous measurements.

The sum can be transformed into:

$$\sum_{i=1}^{N} \frac{(X_i - X_{exp})^2}{\sigma^2{}_{exp}} = \frac{1}{\sigma^2{}_{exp}} \times \left\{ \sum X_i^2 - 2 \times \bar{X} \cdot X_{exp} + N \cdot X_{exp}^2 + N \cdot \bar{X}^2 + N \cdot \bar{X}^2 \; - 2 \cdot N \cdot \bar{X}^2 \right\} =$$

$$\sum_{i=1}^{N} \frac{(X_i - \bar{X})^2}{\sigma^2{}_{exp}} \quad + \quad \frac{N}{\sigma^2{}_{exp}} \cdot \left(\bar{X} - X_{exp}\right)^2 \qquad (2)$$

In (2), the first term is a sum with $N - 1$ degrees of freedom, as the measurement X_i are connected to each other by the value of $\bar{X}$. The first term is proportional to the variance. A test on it is hence a test on the variance.

The second term in (2) has only one degree of freedom and corresponds to the distribution of the average value $\bar{X}$ around the expected value X_{exp} with a standard deviation $\sigma_{exp}/\sqrt{N}$. A test on it is hence a test on the average value.

Because of the way they are derived, the two tests are independent (this can be verified by computer simulations too)

The test on the variance and the test on the average of a set of measurements are completely independent

A Particle Identification based on the Maximum Likelihood can never perform better than a Particle Identification based on the χ^2 test (demonstration)

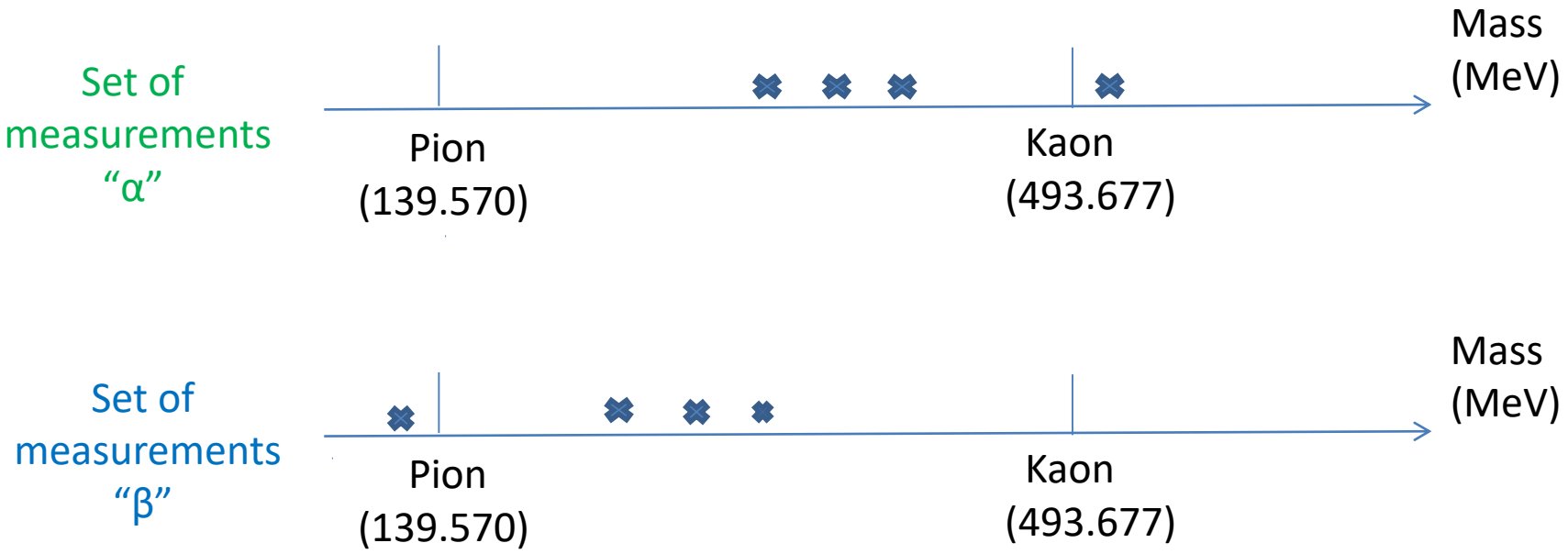

Let us suppose a Kaon crossed the RICH and we detected 4 Čerenkov photons that provided a set of 4 values of its mass. The configuration labelled as Set of measurements "α" has a much bigger probability to happen than its mirror symmetric configuration labelled as Set of measurements "β". The χ^2 test will correctly identify the particle which crossed the RICH, in case the configuration labelled as Set of measurements "α" occurs and will fail, vice versa, if the configuration labelled as Set of measurements "β" occurs. If a Maximum Likelihood Method correctly identifies the particle crossing the RICH as a Kaon, when the configuration labelled as Set of measurements "β" occurs, it will fail, for symmetry reasons, to identify the particle as a Kaon in case the configuration labelled as Set of measurements "α" occurs. Because the configuration labelled as Set of measurements "α" has a bigger probability to happen than the configuration labelled as Set of measurements "β", the Maximum Likelihood Method fails to identify correctly the particle more often than the χ^2 test. This happens because the χ^2 test is anchored to the event probability distribution, while the Maximum Likelihood is not.

An example: the Jlab Hall A RICH used in the experiment E94-108: (hypernuclear spectroscopy)

In the case of the experiment E94-107 in Hall A at Jlab, the detected particle momentum was 1.96 GeV/c and the refractive radiator index was n = 1.29. The Čerenkov photon angles for protons, K^+ and π^+ were respectively:

$$\vartheta_{exp}^{p} = 0.5366 \text{ rad};$$
$$\vartheta_{exp}^{\pi^+} = 0.6645 \text{ rad};$$
$$\vartheta_{exp}^{K^+} = 0.6807 \text{ rad};$$

The variances of the Čerenkov angle distributions around these three distributions were equal to:

$$(\sigma_{exp}^{p})^2 = \quad (\sigma_{exp}^{K^+})^2 = \quad (\sigma_{exp}^{\pi^+})^2 = \sigma^2{}_{exp} = 0.0174 \text{ rad}$$

To identify a particle which crossed the RICH and generated N clusters on the cathode of the proportional chamber, we calculated, for each cluster, the emission angle of the corresponding Čerenkov photon. We obtained in this way N measurements ϑ_i of the particle emitted Čerenkov photon angle. We calculated then the average value $\bar{\vartheta}$ of the N measurements ϑ_i:

$$\bar{\vartheta} = \frac{\sum_{i=1}^{N} \vartheta_i}{N}$$

And the three sums:

$$(\chi^p)^2 = \sum_{i=1}^{N} \frac{\left(X_i - \vartheta_{exp}^{p}\right)^2}{\sigma^2{}_{exp}}; \quad (\chi^{K^+})^2 = \sum_{i=1}^{N} \frac{\left(X_i - \vartheta_{exp}^{K^+}\right)^2}{\sigma^2{}_{exp}}; \quad (\chi^{\pi^+})^2 = \sum_{i=1}^{N} \frac{\left(X_i - \vartheta_{exp}^{\pi^+}\right)^2}{\sigma^2{}_{exp}};$$

To identify a particle detected as K^+, we set a confidence level α_{rej} to consider not acceptable the values of $(\chi^p)^2$ and of $(\chi^{\pi^+})^2$, a confidence level α_{acc} to consider acceptable the value of $(\chi^{K^+})^2$ and a confidence level $\alpha_{accvalmed}$ to consider acceptable the average value $\bar{\vartheta}$ when checked against the expected Kaon Čerenkov emission angle. $\vartheta_{exp}^{K^+}$. Typical values were $\alpha_{rej} = 0.0001$, $\alpha_{acc} = 0.001$ and $\alpha_{accvalmed} = 0.001$.

The χ^2 test as a method to eliminate false signals generated by noise

Very often we are in presence of "false" signals generated by noise/background. Most of these false signals can be identified and eliminated thanks to the χ^2 test. In fact, let us suppose that none of the three sums: $(\chi^p)^2$, $\left(\chi^{K^+}\right)^2$ and $\left(\chi^{\pi^+}\right)^2$ is acceptable. Because, in any case, at least one particle has crossed the RICH, and hence one of the three χ^2 values would have been statistically acceptable, at least one of the signals we are analysing is false. One can hence eliminate 1, 2, …, $N_{removed}$ terms from the sums which define $(\chi^p)^2$, $\left(\chi^{K^+}\right)^2$ and $\left(\chi^{\pi^+}\right)^2$, starting from the biggest ones, until at least one of the three χ^2 values is acceptable. Removing the biggest terms from the sums which define $(\chi^p)^2$, $\left(\chi^{K^+}\right)^2$ and $\left(\chi^{\pi^+}\right)^2$ enhances the probability to eliminate false signals instead of the true ones, because noise signals spread evenly in the RICH while true signals cluster around the expected value. In the hypernuclear spectroscopy experiments we were able to eliminate noise signals which amounted to 25% of the total signals. In the transversity experiment we were able to eliminate noise signals which amounted to 75% of the total signals. With method based on the calculation of the average of the signals or on the Maximum Likelihood, the elimination of noise signals is impossible.

Results (experiment E94-108):

Inefficacy of the signal average calculation:
in presence of noise:

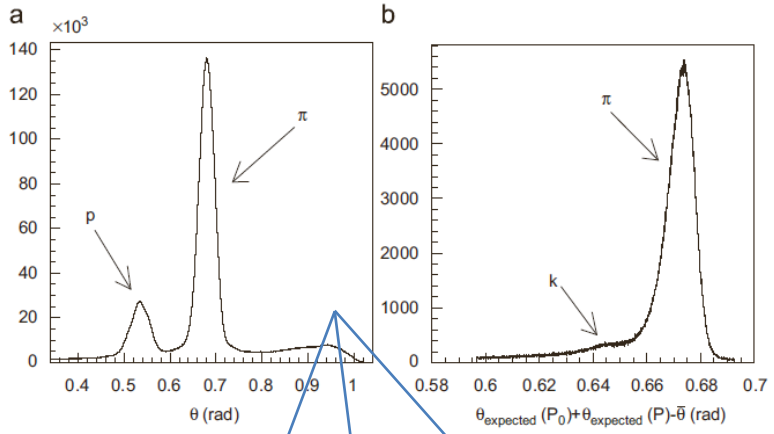

ϑ_i distribution $\bar{\theta}$distribution

Effectiveness of the χ^2test and of the test on the average performed simultaneously:

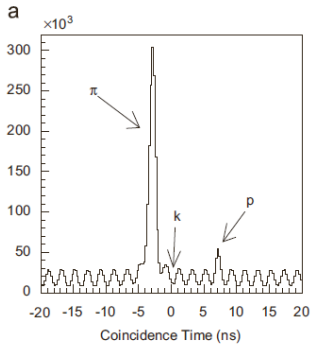

No RICH PID

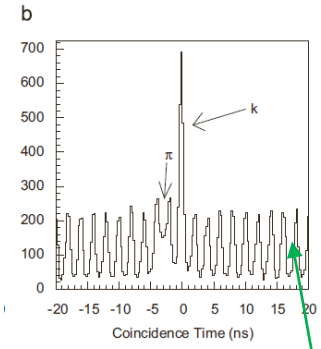

Both $\left(\chi^{\pi^+}\right)^2$ and $\bar{\vartheta} - \vartheta_{\mathrm{exp}}^{\pi^+}$ probabilities < 0.0001 and both $\left(\chi^{K^+}\right)^2$ and $\bar{\vartheta} - \vartheta_{\mathrm{exp}}^{K^+}$ probabilities > 0.1

$\pi^+/_{K^+}$ rejection ratio $= 340 \pm 11$;
K^+ detection efficiency ~ 91%

χ^2test effectiveness (without average value test):

π^+rejection ~ 100%;
K^+ detection efficiency ~ 70%

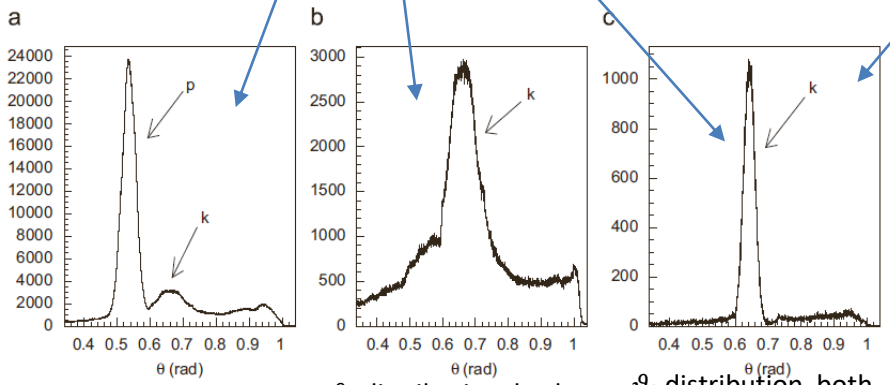

ϑ_i distribution $\left(\chi^{\pi^+}\right)^2$ probability < 0.0001

ϑ_i distribution, both $\left(\chi^{\pi^+}\right)^2$ and $(\chi^p)^2$ probabilities < 0.0001

ϑ_i distribution, both $\left(\chi^{\pi^+}\right)^2$ and $(\chi^p)^2$ probabilities < 0.0001 and $\left(\chi^{K^+}\right)^2$ probability > 0.1

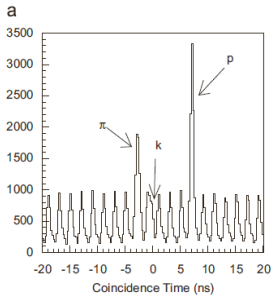

Two Čerenkov detector cuts only

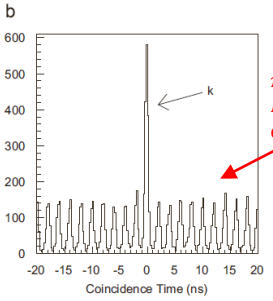

π^+rejection ~ 100%;
K^+ detection efficiency ~ 96%

Two Čerenkov detector cuts; $\left(\chi^{\pi^+}\right)^2$ probability < 0.01; $(\chi^p)^2$ probability < 0.0001 and $\left(\chi^{K^+}\right)^2$ and both $\left(\chi^{K^+}\right)^2$ and $\bar{\vartheta} - \vartheta_{\mathrm{exp}}^{K^+}$ probabilities > 0.001

Radiative effect subtraction

(general concept, rigorous mathematical demonstration in PHYSICAL REVIEW C **91**, 034308 (2015)

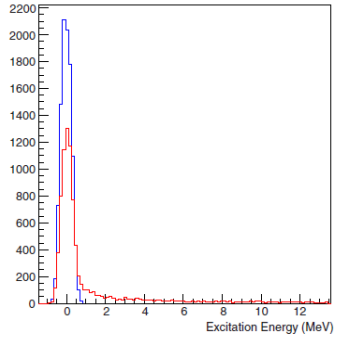

Figure A

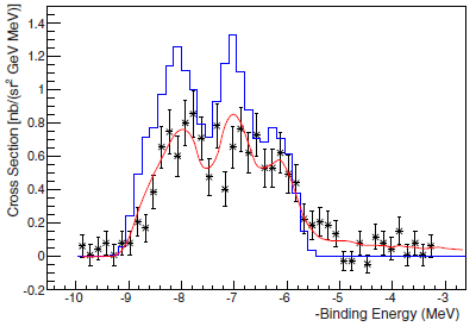

Figure B

From Figure A above you see that the resolution of a binding energy spectrum is spoiled by radiative effects. The blue curve in Figure A shows an hypothetical binding energy spectrum peak in absence of radiative effects. The red curve in the same figure shows as the peak shown by the blue curve transforms because of radiative effects. Let us call "Radiative effect function" the function which transform the blue curve into the red curve in Figure A. The blue curve in Figure B above shows the spectrum you would have obtained if radiative effects had not existed. The point with errors in Figure B shows the measured experimental spectrum, which is given by the convolution of the blue curve with the "Radiative effect function". Let us call "Pure spectrum" the binding spectrum you would have obtained in absence of radiative effects and "Experimental spectrum" the experimental spectrum you have obtained. To a certain "Pure spectrum" will correspond one and only one "Experimental spectrum" because the "Radiative effect function" is unique. It is true the vice versa: to a certain "Experimental spectrum" it will correspond one and only one "Pure spectrum". This because the experimental spectrum is made up even by hundreds of bins while the number of peaks is generally limited. It hence impossible, in practice, find two different "Pure spectrums" which generate the same "Experimental spectrum". The "Radiative effects function" is well known and is incorporated in Monte Carlos. Let us suppose that your "Experimental spectrum" has a poor resolution energy that forbids to clearly identify peaks. If a Monte Carlo is able to fit your "Experimental spectrum" with "Radiative effects turned on" (as shown by the red curve in Figure B), even starting by a peak configuration that is just an hypothesis, this Monte Carlo will provide the correct "Pure Spectrum" when it is run with "Radiative effects turned off". If this had not be true, it would have meant that two different "Pure spectrum" would have been able to give the same "Experimental spectrum" and this is impossible as quoted above. The obtained "Pure spectrum" has a much better resolution and can be analyzed easily.

TABLE IV. Columns 2 and 3 give peak positions and relative amplitudes of five configurations α, β, γ, δ, and ϵ for which the Monte Carlo SIMC predicts a ${}^{9}_{\Lambda}$Li excitation energy spectrum that fits the experimental data. Column 4 lists the χ^2 test values calculated through Eq. (A13) for these configurations.

Configuration	Peak Positions MeV	Peak Amplitudes Arbitrary units	χ^2 35 ndf
	0.00	2.23	
	0.64	3.54	
α	1.32	1.90	36.685
	1.71	2.61	
	2.35	2.33	
	0.00	2.08	
	0.58	3.48	
β	1.54	3.38	38.247
	2.37	2.10	
	0.00	2.34	
	0.54	3.88	
γ	1.49	3.78	46.088
	2.36	3.28	
	0.00	1.86	
	0.54	3.08	
δ	1.49	3.00	39.068
	2.36	2.06	
	0.00	1.85	
	0.65	3.09	
ϵ	1.43	3.00	39.000
	2.39	2.06	

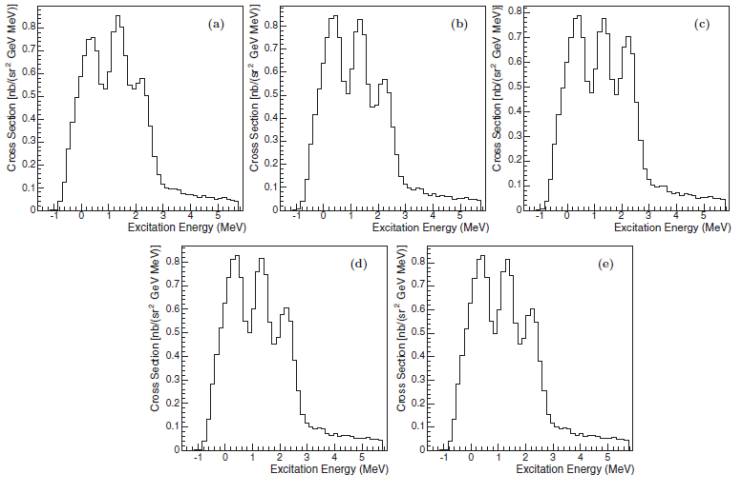

FIG. 6. ${}^{9}_{\Lambda}$Li excitation energy spectra as predicted by the Monte Carlo SIMC for the peak configurations α, β, γ, δ, and ϵ quoted in Table IV [panels (a)–(e), respectively].

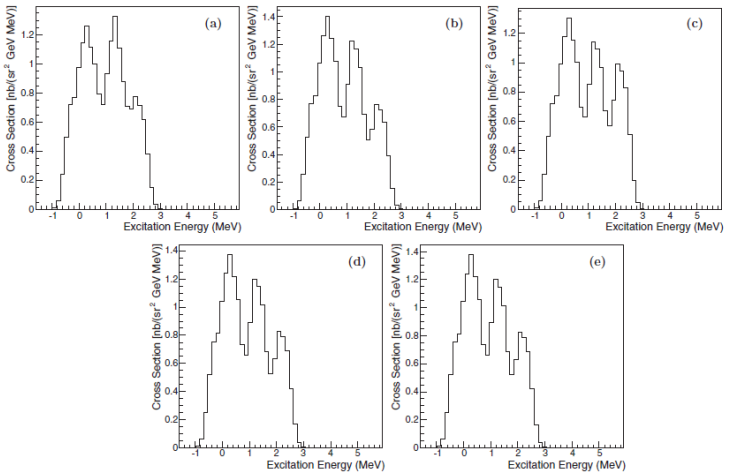

FIG. 7. ${}^{9}_{\Lambda}$Li excitation energy spectra as predicted by the Monte Carlo SIMC for the peak configurations α, β, γ, δ, and ϵ quoted in Table IV when the radiative effects are "turned off" [panels (a)–(e), respectively].

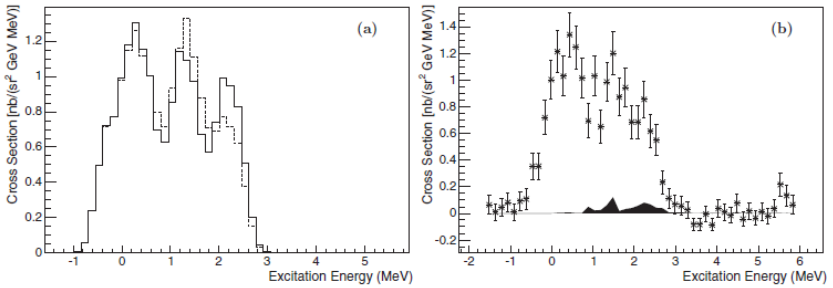

FIG. 8. (a) The spectrum of the configuration α (dashed line) and of the configuration γ (continuous line) as predicted by the Monte Carlo SIMC when the radiative effects are turned off. (b) The statistical errors (error bars) and the systematic errors (full band) as a function of the excitation energy. The systematic error was defined as the difference between the dashed line and the continuous line of panel (a); see text for details.

Experimental results

The elementary reactions $p(e,e')\Lambda$

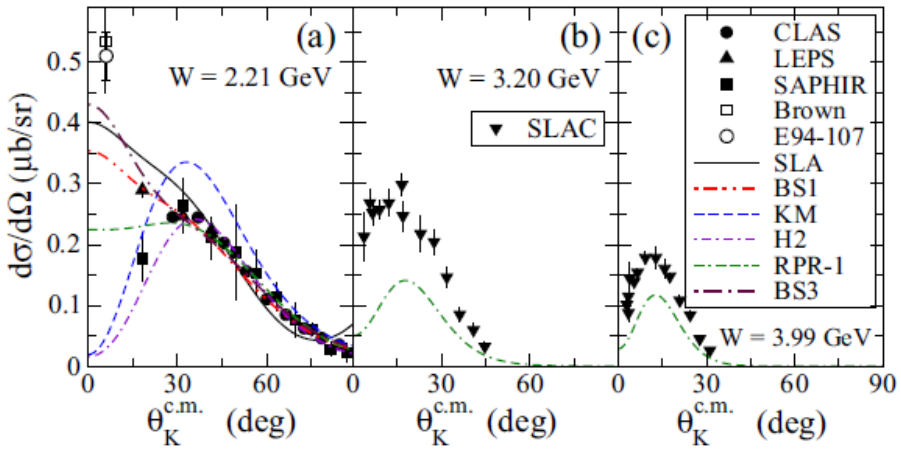

Electroproduction results superimposed on the photoproduction data are plotted. Also shown are predictions for photoproduction of several models. The results of the models markedly differ for kaon angles smaller than 30°. The relevant difference in dynamics of the presented models is in their description of the nonresonant part of the amplitude. The SLA isobar model does not assume any hadronic form factors but instead includes exchanges of hyperon resonances to suppress contributions from the Born terms. The model KM includes hadronic form factors without any hyperon resonances and the H2, BS1, and BS3 models include both hyperon resonances and hadronic form factors. The strong suppression of the nonresonant part at very small angles is apparent when the hadronic form factors are used with or without a small number of hyperon resonances, as in the H2
and KM models, respectively. On the contrary, in the recent isobar models BS1 and BS3, an ample number of hyperon resonances with spin 1/2 and 3/2 contribute to the nonresonant part of the amplitude that results in a similar behavior of the cross section at $\vartheta_k^{c.m} < 30°$ as for the SLA model in the Figure. In the Regge-plus-resonance model RPR-1, the nonresonant part is given by the Regge trajectories without any hadronic form factors.

${}^{9}_{\Lambda}Li$ data

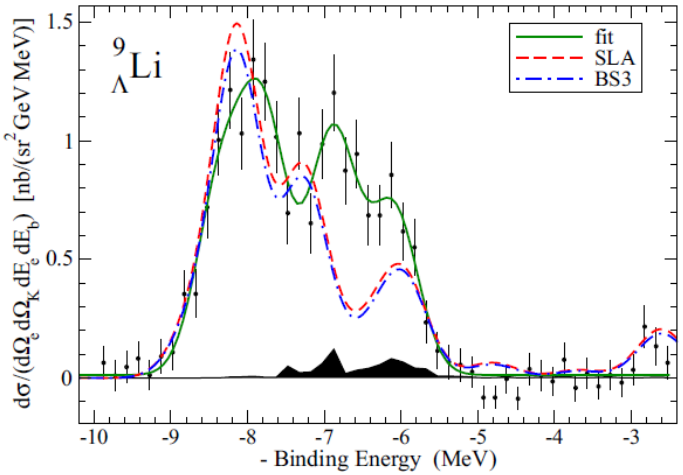

Experimental data			Theoretical predictions			
E_x (MeV)	Width (FWHM) (MeV)	Cross section [nb/(sr^{2}GeV)]	E_x (MeV)	J^π	Cross section [nb/(sr^{2}GeV)]	Cross section sum
0.00 ± 0.08	0.73 ± 0.06	0.59 ± 0.15	0.00	$3/2^+$	0.18	1.22
0.57 ± 0.12	0.73 ± 0.06	0.83 ± 0.13	0.59	$5/2^+$	1.04	
1.47 ± 0.09	0.73 ± 0.06	0.79 ± 0.07	1.43	$3/2^+$	0.29	0.59
			1.45	$1/2^+$	0.30	
2.27 ± 0.09	0.73 ± 0.06	0.54 ± 0.06	2.27	$5/2^+$	0.17	0.48
			2.74	$7/2^+$	0.31	

034308-5

There is some disagreement between the DWIA calculation with a standard model of *p* shell hypernuclei and the measurements, both for the position of the peaks and for the cross sections. In fact, the theory predicts a larger ratio of the cross sections for the members of the ground-state doublet and a larger spacing between the second and third doublets. The $5/2^+$ state is predicted to be dominantly populated because of the structural dominance of spin flip and the strong dominance of the spin-flip part of the elementary amplitude at very small production angles ($\vartheta_{K\gamma}$ =1.8°). The predicted theoretical cross sections are 10–20% below the experimental values, probably because of uncertainties in the elementary-production operator. The structure calculations of doublet properties are generally in agreement with data. There are disagreements for the spacing between doublets. These depend mainly on S_N and perhaps also on the three body *ΛNN* interaction that has not yet been included in the shell-model calculations. The cross sections depend on the spectroscopic factors for proton removal from the target.

$^{12}_{\Lambda}B$ data

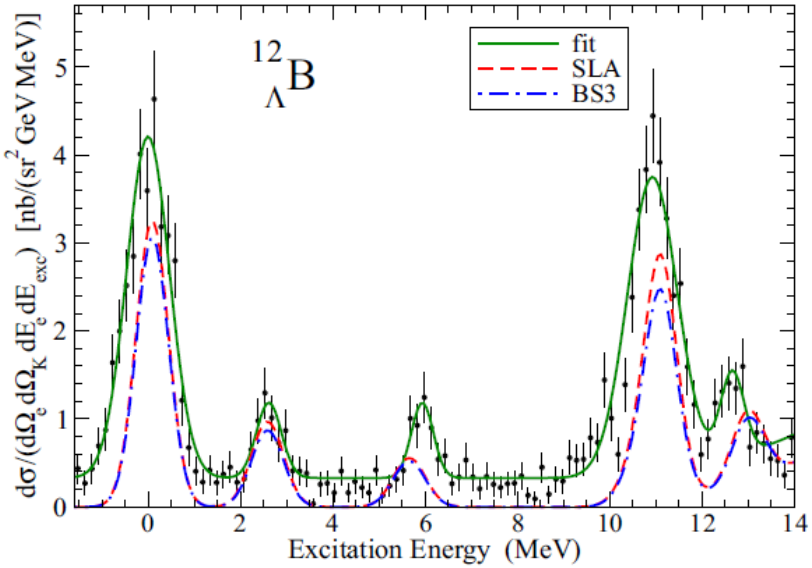

Experimental data			Theoretical cross sections					
E_x	Width (FWHM)	Cross section	E_x	J^π	SLA		BS3	
(MeV)	(MeV)	[nb/(sr^{2}GeV)]	(MeV)		[nb/(sr^{2}GeV)]	Sum	[nb/(sr^{2}GeV)]	Sum
0.00 ± 0.03	1.09 ± 0.05	4.51 ± 0.23 ± 0.67	0.00	1^-	0.640		0.524	
			0.116	2^-	2.227	2.87	2.172	2.70
2.62 ± 0.06	0.64 ± 0.11	0.58 ± 0.10 ± 0.11	2.587	1^-	0.846		0.689	
			2.593	0^-	0.001	0.85	0.071	0.76
5.94 ± 0.06	0.56 ± 0.10	0.51 ± 0.09 ± 0.09	5.642	2^-	0.368		0.359	
			5.717	1^-	0.119	0.49	0.097	0.46
10.93 ± 0.04	1.29 ± 0.07	4.68 ± 0.24 ± 0.60	10.480	2^+	0.194		0.157	
			10.525	1^+	0.085		0.100	
			11.059	2^+	0.959		0.778	
			11.132	3^+	1.485		1.324	
			11.674	1^+	0.050	2.77	0.047	2.41
12.65 ± 0.06	0.60 ± 0.11	0.63 ± 0.12 ± 0.15	12.967	2^+	0.552		0.447	
			13.074	1^+	0.167	0.72	0.196	0.64

Five peaks are observed in the spectrum. The main ones are the g.s. peak and the *p*-shell peak at 10.93 MeV. The peak at E_x=5.94 MeV has the narrowest width (560 keV). The two main peaks have widths larger suggesting that they are composed of two or more peaks separated by a noticeable excitation energy. States with an s_Λ coupled to excited ^{11}B core states are clearly observed between the g.s. and the peak at 10.93 MeV with signal-to-noise ratios larger than 5. The positions of these levels were determined with uncertainties of less than 100 keV. This states are observable because the spin-spin interaction enhances their cross sections with respect to the weak-coupling limit. The comparison with the data shows that theory mostly underpredicts the cross sections by 20–40%,

$^{16}_{\Lambda}N$ data

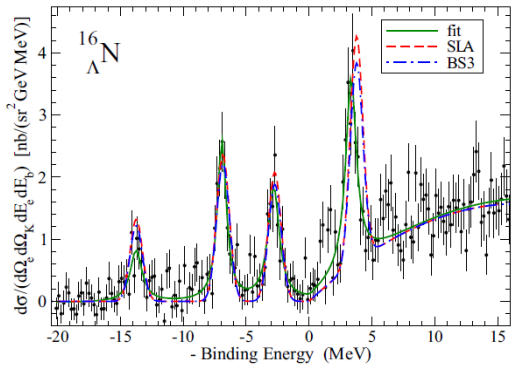

FIG. 20. The $^{16}_{\Lambda}$N binding-energy spectrum. The solid line shows the best fit using Voigt functions (see text for details). The theoretical curves (dashed and dash-dotted lines) were calculated with an average width extracted from the fit (FWHM = 1177 keV).

Experimental data			Theoretical prediction			
E_x (MeV)	Width (FWHM, MeV)	Cross section (nb/sr^2/GeV)	E_x (MeV)	Wave function	J^π	Cross section (nb/sr^2/GeV)
0.00	1.71 ± 0.70	1.45 ± 0.26	0.00	$p_{1/2}^{-1} \otimes s_{1/2\Lambda}$	0^-	0.002
			0.03	$p_{1/2}^{-1} \otimes s_{1/2\Lambda}$	1^-	1.45
6.83 ± 0.06	0.88 ± 0.31	3.16 ± 0.35	6.71	$p_{3/2}^{-1} \otimes s_{1/2\Lambda}$	1^-	0.80
			6.93	$p_{3/2}^{-1} \otimes s_{1/2\Lambda}$	2^-	2.11
10.92 ± 0.07	0.99 ± 0.29	2.11 ± 0.37	11.00	$p_{1/2}^{-1} \otimes p_{3/2\Lambda}$	2^+	1.82
			11.07	$p_{1/2}^{-1} \otimes p_{1/2\Lambda}$	1^+	0.62
17.10 ± 0.07	1.00 ± 0.23	3.44 ± 0.52	17.56	$p_{3/2}^{-1} \otimes p_{1/2\Lambda}$	2^+	2.10
			17.57	$p_{3/2}^{-1} \otimes p_{3/2\Lambda}$	3^+	2.26

Four peaks are observed in the spectrum. The ground state peak gives a separation energy of B=13.76 ± 0.16 (stat.) ± 0.04 (syst.) MeV for the 1^- member of the ground-state doublet.Three more peaks are observed at binding energies of 6.93, 2.84, and −3.34 MeV. The theory overpredicts the cross sections by 10–30%, contrary to the case of $^{12}_{\Lambda}B$ and $^{9}_{\Lambda}Li$ production. This opposite tendency of the hypernuclear cross sections can be hardly attributed to uncertainties in the elementary production cross sections but is more likely due to the use of simple hole states for the ^{15}N core nucleus

Conclusions

The experiment E94-107 performed the study of binding and/or excitation energy spectra of the hypernuclei ${}^{9}_{\Lambda}Li, {}^{12}_{\Lambda}B$, and ${}^{16}_{\Lambda}N$. To make this experiment run very important upgrades of the standard Hall A apparatus were needed, namely the addition of two septa to make HRSs being able to detect particles scattered at very forward angles and the addition of a RICH detector to the detector package of one HRS in order to obtain a PID able to eliminate the very big pion and proton background. Innovative analysis algorithms were needed to optimize the optic databases of the spectrometers employed, to achieve a very good PID and to obtain the desired resolution. Interesting data were achieved which prompt theoreticians to refine their tools of analysis and the experimentalists to further continue their investigations with the study of binding energy spectra of other hypernuclei